

Spectroscopic analysis of a super-hot giant flare observed on Algol by BeppoSAX on 30 August 1997

F. Favata¹ and J. H. M. M. Schmitt²

¹ Astrophysics Division – Space Science Department of ESA, ESTEC, Postbus 299, NL-2200 AG Noordwijk, The Netherlands

² Universität Hamburg, Hamburger Sternwarte, Gojenbergsweg 112, D-21029 Hamburg, Germany

Received 21 June 1999; accepted 4 August 1999

Abstract. We present an X-ray observation of the eclipsing binary Algol, obtained with the BeppoSAX observatory. During the observation a huge flare was observed, exceptional both in duration as well as in peak plasma temperature and total energy release. The wide spectral response of the different BeppoSAX instruments, together with the long decay time scale of the flare, allowed us to perform a detailed time-resolved X-ray spectroscopic analysis of the flare. We derive the physical parameters of the emitting region together with the plasma density applying different methods to the observed flare decay. The X-ray emission from the flare is totally eclipsed during the secondary optical eclipse, so that the size of the emitting region is strongly constrained (as described in a companion paper) on purely geometrical arguments. The size of the flare thus derived is much smaller than the size derived from the analysis of the evolution of the spectral parameters using the quasi-static cooling formalism, showing that the time evolution of the flare is determined essentially from the temporal profile of the heating, with the intrinsic decay of the flaring loop having little relevance. The analysis of the decay with the technique recently developed for solar flares by Reale et al. (1997) on the other hand is in much better agreement with the eclipse-derived constraints.

The very high signal-to-noise of the individual spectra strongly constrains some of the derived physical parameters. In particular, very significant evidence for a three-fold increase in coronal abundance and for a large increase in absorbing column density during the initial phases of the flare evolution is present.

Key words: Stars: individual: Algol – late-type – activity – coronae – X-rays: stars

1. Introduction

Algol-type systems are short-period eclipsing binaries composed of an early-type primary and a (near) main-sequence late-type secondary. The short orbital period ensures that both

stars are tidally-locked fast rotators. The secondaries in these systems show strong magnetic activity with copious X-ray emission. While tidally-induced activity is a common characteristic in RS CVn-type systems, the early-type primary in Algol-type systems, lacking a surface convective envelope, is not expected to be able to sustain a dynamo. Therefore the coronal structures should be concentrated on the secondary only, making for a simpler geometry and avoiding the complication of cross-system loop structures which may exist in the case of RS CVn-type binaries. Because of its proximity (28.46 pc on the basis of the Hipparcos parallax, ESA 1997) the eponymous system Algol is one of the apparently strongest coronal X-ray sources in the sky.

Its brightness ($V \simeq 2.7$) soon made the periodic fading obvious (it was first reported, in the western world, by Gemignano Montanari in 1667), and their interpretation in terms of mutual eclipses in a binary system was already proposed by John Goodricke in 1782. The system consists of a B8 V primary and a K2 IV secondary (plus a more distant tertiary component, with a period of $\simeq 1.8$ yr and a spectral type A or F). Hill et al. (1971) report values for the masses and radii of the two components $R_A = 3.0 R_\odot$, $M_A = 3.7 M_\odot$ and $R_B = R_K = 3.4 R_\odot \simeq 2.4 \times 10^{11}$ cm, $M_B = 0.8 M_\odot$, while Richards (1993) reports $R_A = 2.90 R_\odot$, $M_A = 3.7 M_\odot$ and $R_B = R_K = 3.5 R_\odot \simeq 2.5 \times 10^{11}$ cm, $M_B = 0.81 M_\odot$; the orbital inclination is reported to be $i = 81.4$ deg. We will adopt the Richards (1993) parameters in the following. The orbital period is $\simeq 2.8673$ d. The ephemeris we have adopted in the present work is HJD 2 445 739.0030 + 2.8673285 E (Kim 1989; Al-Naimiy et al. 1985). The separation is $14.14 R_\odot$, or $\simeq 4$ times the radius of the K star.

Algol was identified as an X-ray source already in the '70s with observations from the SAS 3 satellite (Schnopper et al. 1976) and its soft X-ray emission was confirmed with sounding rocket flights (Harnden et al. 1976). Its intense activity level has made it a target of choice for most UV, EUV and X-ray observatories. The high level of X-ray emission was initially interpreted in the framework of the mass-transfer paradigm, given the evidence from optical data of mass transfer taking place between the two components (see Richards 1993 and references therein). However, spectroscopic observations soon showed a hot, thermal X-ray spectrum, requiring the presence of magnet-

ically confined plasma, i.e. of a corona, expected to be located on or around the K-type secondary.

The soft X-ray emission of Algol is characterized by the frequent occurrence of major flares. Almost all sufficiently long observations to date have yielded a significant flaring event, with EXOSAT (White et al. 1986; van den Oord & Mewe 1989), GINGA (Stern et al. 1992) and ROSAT (Ottmann & Schmitt 1996) all observing long-lasting flares (with effective decay times ranging between 5 and 20 ks), which have been extensively discussed in the literature. The above flares have all been analyzed in a similar way, allowing for a reasonably homogeneous comparison of their characteristics to be made. In particular, the observed decay has in all cases been used to derive (following the formulation of van den Oord & Mewe 1989) the length, and consequently, the average density of the flaring plasma, under the assumption that the flaring loop evolves through a series of “quasi-static” loop states. In all cases the analysis has made use of the observed constancy of the normalized ratio between the radiative and conductive cooling time μ (see Sect. 5.2) to ascertain that the flaring loop(s) are cooling through a sequence of quasi-static states, and of the small value of the heating function present as a parameter in the quasi-static formalism to establish the lack of additional heating during the flare decay phase.

The loop lengths¹ thus derived range between 1 and 6×10^{11} cm (i.e. between 0.4 and $2.4 R_K$ – see Table 3). These large loops (comparable or larger in size than the stellar radius, unlike the solar case, in which flaring structures are small compared to the solar radius) are however shorter than the coronal pressure scale height because of their high temperatures and the low surface gravity of the K-type subgiant Algol secondary. The corresponding plasma densities, derived within the same framework, range between 5 and $26 \times 10^{10} \text{ cm}^{-3}$. The general picture for the flaring regions observed on Algol is therefore one of large and rather tenuous loops, a natural consequence of the very energetic and long-lasting flares if no heating is indeed present during the decay phase. In the solar case, in addition to the “compact” flares, in which the plasma appears to be confined to a single loop whose geometry does not significantly evolve during the event, a second class of flares is usually recognized, i.e. the “two-ribbon” flares, in which a disruptive event appears to open up an entire arcade of loops, which subsequently closes back, leading to the formation of a growing system of loops whose footpoints are anchored in H α -bright “ribbons”. Two-ribbon flares are generally characterized by a slower rise and decay, and a larger energy release. Compact flares have often been considered to be due to “impulsive” heating events, while the longer decay times of two-ribbon events have been considered as a sign of sustained heating. However, also in the case of compact flares sustained heating has been shown to be frequently present (Reale et al. 1997), so that the distinction may indeed be less clear than often thought.

¹ All along the present paper, the term “loop length” will be used to indicate the length from the footpoint to the apex of the loop, i.e. actually its “semi-length”.

Long-lasting stellar flares have at times considered as analogs to solar two-ribbon flares (due to their longer time scales, e.g. Pallavicini et al. 1990). However, the only available theoretical framework so far available to model this type of event (Kopp & Poletto 1984) relies on a large number of free parameters and assumptions (such as the conversion efficiency of the magnetic field into X-rays and the assumption of instantaneous dissipation of the reconnection energy). As a consequence the physical parameters of the flaring regions derived with this approach are, for spatially unresolved events such as the stellar ones, rather strongly dependent on some specific assumptions, so in practice most stellar flares have been modeled as compact events. We will follow the same approach here, however keeping in mind the possibility that the event may not be necessarily described as a compact one.

We have performed a long ($\simeq 240$ ks elapsed time, covering a full orbit of the system) observation of Algol with the BeppoSAX X-ray observatory, aiming at studying both the spectral and the temporal characteristics of its X-ray emission. During the observation a very large and long-lasting flare was observed. We present in this paper a detailed analysis of the characteristics of this flare, deriving the temporal evolution of the spectral parameters of the plasma (temperature T , emission measure EM , coronal abundance Z , absorbing column density $N(\text{H})$), and subsequently applying different methods to the analysis of the flare decay in order to derive the physical characteristics of the flaring region. For this purpose we have applied both the quasi-static decay method of van den Oord & Mewe (1989) and the method of Reale et al. (1997), which allows for the possibility of (exponentially decaying) sustained heating during the flare decay, and simultaneously deriving both the time scale of heating and the size of the flaring loop. In line with the previous analyses of large flares on Algol, the analysis of the flare’s decay using the quasi-static approach results in a long and tenuous flaring loop, although in this case the derived loop size and density are more extreme given the exceptionally long duration and peak temperature of the event.

One unique characteristic of the flare studied here is that its emission underwent a total eclipse coincident with the secondary optical eclipse. This allows (as discussed in detail in a companion paper, Schmitt & Favata 1999) to put a firm upper limit to the size of the flaring region, and thus to compare, for the first time in a context other than the solar one, the length derived through the analysis of the flare decay with the geometrical size of the emitting region.

This comparison shows that the loop sizes derived from the analysis of the flare decay through the quasi-static method are significantly larger than the geometrical size of the flaring region. Therefore the actual flaring region must have had a much larger plasma density, and sustained heating must have been present during all the decay phase to explain the long observed decay time. The method of Reale et al. (1997) produces a large range of allowed loop lengths, which at the lower end overlap with the size derived for the flaring region from the eclipse

analysis. Also, this type of analysis points to the presence of significant sustained heating during the decay phase.

The metal abundance of the flaring plasma is seen to vary significantly during the course of the flare's evolution. Abundance variations during the evolution of the flare were already hinted at in the analysis of the GINGA (Stern et al. 1992) and ROSAT (Ottmann & Schmitt 1996) flares, and evidence for this type of effect has been reported for flares on other stars. The combination of high statistics, good spectral resolution and wide spectral coverage of the present Algol observation make it however possible for the first time to quantitatively derive the evolution of the plasma abundance. Finally, large variations of absorbing column density are also observed during the early evolution of the flare, hinting at the possibility of a coronal mass ejection taking place in association with the onset of the flare.

Although flares of different types from several classes of coronal sources have been discussed in detail in the literature in the past, the large flaring event on Algol discussed in the present paper is exceptional for several reasons:

- Its long duration (almost two days) associated with its high luminosity allows for high signal-to-noise spectra to be collected with a time resolution small compared with the time scale of flare evolution, and thus to analyze in detail the temporal evolution of the plasma parameters with small statistical errors, and on different time scales.
- The complete, uninterrupted time coverage, from several thousand seconds before the onset of the flare until the end of its decay allows for its complete temporal evolution to be studied.
- The occurrence of a *total* eclipse of the flaring plasma by the primary star allows, for the first time, for a geometrical determination of the size of the flaring structure (see Schmitt & Favata 1999), which can then be compared with the loop lengths derived through an analysis of the decay of the spectroscopic parameters. This allows for a critical test of the assumptions underlying these techniques, which are the only ones available when confronted with stellar flares with no spatial resolution.
- The high X-ray flux and spectral temperature associated with this event, together with the unprecedented energy coverage offered by the instrumental complement of the BeppoSAX observatory allow for the spectrum of the flaring plasma to be studied between 0.1 and 100 keV, thus removing the uncertainties on the temperature of the flaring plasma during the hottest phases of large flares (where even the ASCA instruments can only provide lower limits to the temperature) which have characterized previous analyses of large flares. At the same time, the spectral shape can be critically determined, in particular looking for the presence of non-thermal spectral components.

2. The BeppoSAX observation

The BeppoSAX observatory (Boella et al. 1997a) features different instruments, four of which were used in the analysis of

our Algol observation, i.e. the LECS (Parmar et al. 1997, which covers the energy range 0.1–10 keV), the two MECS detectors (Boella et al. 1997b, MECS-2 and MECS-3, covering the range 1.6–10 keV) and the PDS detector (Frontera et al. 1997, covering between 15 and 300 keV – only data in the 15–100 keV band were used in the present paper).

The BeppoSAX observation of Algol covered a complete binary orbit (i.e. $\simeq 240$ ks elapsed time). It started on Aug. 30, 1997 at 03:04 UT (shortly before the primary optical eclipse) and lasted until Sep. 1, 1997 at 20:32 UT. Approximately 20 ks after the beginning of the observation, a very strong flare began, whose evolution dominates the rest of the observation.

A detailed analysis of the total eclipse of the flare as seen in the MECS detectors is presented by Schmitt & Favata (1999), who derive the corresponding geometrical constraints on the size and shape of the flaring region. The present paper will concentrate on the spectral analysis of the X-ray emission and on the analysis of the characteristics of the flaring region from the flare decay, using the complete spectral range covered by the BeppoSAX detectors.

2.1. Data reduction

Telemetry files, containing both information on individual detected X-ray photons and house-keeping data were obtained from the observation tapes for each instrument, and data for each instrument were individually processed with the SAXDAS software (available from the BeppoSAX Scientific Data Center – hereafter SDC, reachable at <http://www.sdc.asi.it>), with the default settings, producing FITS-format linearized photon event files for each instrument.

For the three imaging instruments (LECS, MECS-2, MECS-3) standard extraction regions were used, i.e. 8.2 and 4.0 arcmin diameter circles centered on the source, for the LECS and MECS data, respectively. The background was extracted from regions of the same size and location as the source extraction region from the standard background files supplied by the SDC. Spectra and light-curves both for the source and the background were extracted using the XSELECT software. PDS spectra and light-curves were extracted using the SAXDAS-supplied packages, which directly produce background-subtracted spectra and light-curves.

2.2. Light curves

The background-subtracted light-curve in the 15–100 keV band, extracted from the PDS data, is shown in Fig. 1, binned in 6000 s intervals, while the background-subtracted light-curve in the 1.6–10.0 keV band, extracted from the MECS-3 detector is shown, binned in 600 s intervals, in Fig. 2. The light-curve for a softer band (0.1–0.5 keV) derived from the LECS data is shown in Fig. 3, binned in 900 s intervals. The LECS is operated during Earth night only, resulting in a lower observing efficiency and in the larger data gaps seen in Fig. 3 with respect to Fig. 2.

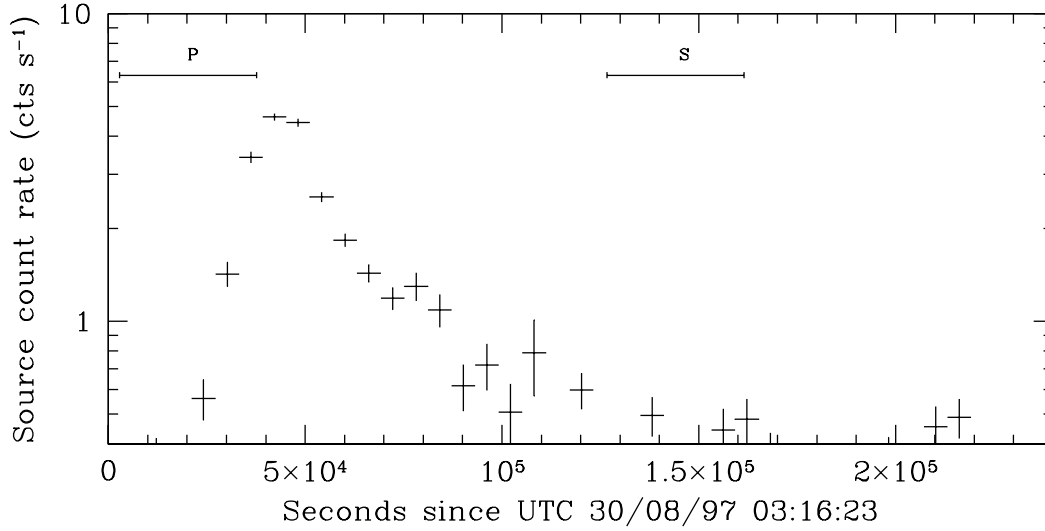


Fig. 1. The light-curve of the Algol observation of BeppoSAX in the 15–100 keV band, as measured in the PDS detector, binned in 6000 s intervals. The location and duration of the primary and secondary optical eclipse, using the ephemeris of Kim (1989), is also plotted.

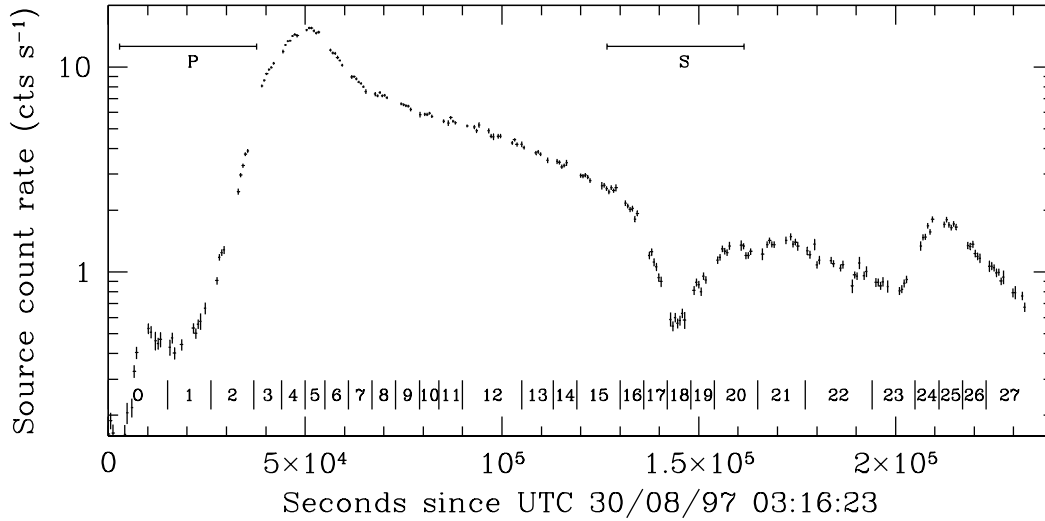


Fig. 2. The light-curve of the Algol observation of BeppoSAX in the 1.6–10 keV band, as measured in the MECS-3 detector, binned in 600 s intervals. The vertical lines indicates the boundaries of the time segments in which the observation has been broken for the purpose of performing time-resolved spectroscopy. The location and duration of the primary and secondary optical eclipse, using the ephemeris of Kim (1989), is also plotted.

Inspection of Fig. 2 shows that the flare (as seen in the 1.6–10 keV band) has a rather slow rise (with ≈ 30 ks between the flare start and the peak). The decay is for the first ≈ 15 ks relatively rapid, on time scales comparable with the rise, but then slows down becoming very nearly exponential. The eclipse due to secondary is well visible, between ≈ 130 and ≈ 160 ks from

the beginning of the observation. The exponential decay is interrupted, at ≈ 200 ks, by the onset of yet another flare.

The hard (15–100 keV) X-ray light curve shows a slow rise, similar to the one seen in the 1.6–10 keV band, but a faster decay. The hard X-ray count rate returns to its pre-flare value at ≈ 130 ks from the beginning of the observation, so that the eclipse of the flaring plasma is not visible in this band. Also,

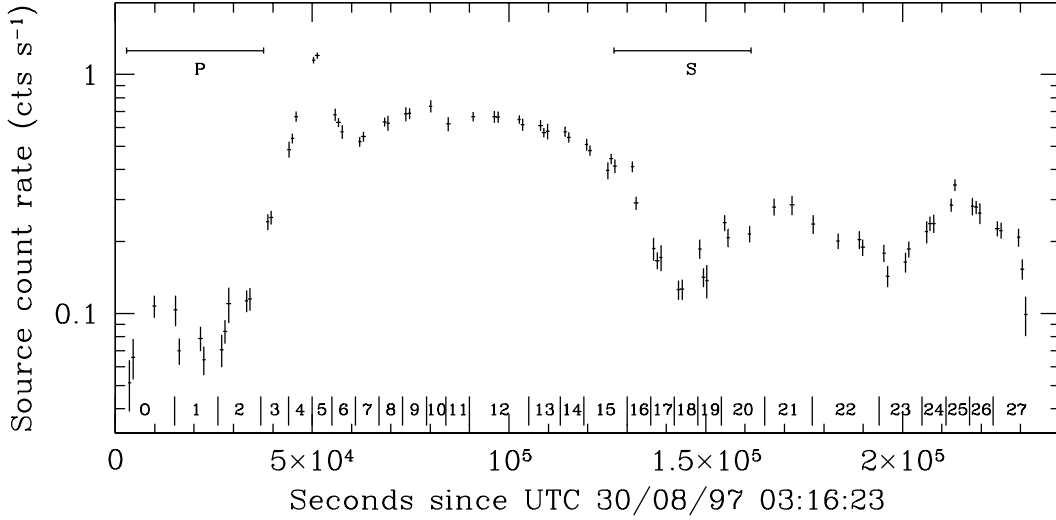


Fig. 3. The light-curve of the Algol observation of BeppoSAX in the 0.1–0.5 keV band, as measured in the LECS detector, binned in 900 s intervals. The vertical lines indicates the boundaries of the time segments in which the observation has been broken for the purpose of performing time-resolved spectroscopy. The location and duration of the primary and secondary optical eclipse, using the ephemeris of Kim (1989), is also plotted.

there is no evidence for hard pre-flare emission, which could in principle have been due to non-thermal emission associated with fast particles.

The soft-band (0.1–0.5 keV) light curve differs significantly from the 1.6–10 keV band light curve, as the rise is slower, and the decay “bounces back”, after $\simeq 10$ ks, for $\simeq 20$ ks. These differences are discussed in more detail in Sect. 4.2.

2.3. Spectra

The high-count rate of the Algol observation in the LECS and MECS detectors allows for detailed time-resolved spectroscopy. The observation has therefore been split in 28 separate time intervals, with boundaries coinciding with observational gaps due to the Earth blocking the source, and with each segment covering one or more spacecraft orbits. The extent of each time segment is shown, together with a number used in the following to refer to them, in Figs. 2 and 3, together with the light-curve of the observation as measured in the MECS-3 and LECS detectors respectively. The time of optical eclipses is also indicated.

Individual spectra have been extracted, in the LECS, MECS and PDS detectors, for each of the time intervals indicated in Fig. 2. Standard response matrices have been used to analyze the MECS spectra (again as available from the SDC), while the LECS response matrix was computed using the LEMAT program. The standard PDS pipeline already produces background-subtracted spectra and thus no further manipula-

tion was necessary. The standard SDC-provided response matrix has been used to fit the PDS spectra.

All the spectral analysis described here has been performed using the XSPEC version 10.00 software. Each of the individual LECS and MECS spectra accumulated during the intervals marked in Fig. 2 has been rebinned, prior to fitting, to have at least 20 counts per (variable-size) bin, and the statistical weight of each bin for the purpose of determining the χ^2 has been determined using the statistic of Gehrels (1986), more appropriate than the Gaussian approximation for small number of events.

Due to a known discrepancy between the normalization of the response matrices for the LECS and MECS detectors, when LECS and MECS data are fit together it is necessary to add a relative normalization factor to the fit, with experience showing that the MECS normalization is about 10 to 20% higher than the LECS one. It is not possible however to determine a priori the exact value of the normalization, as this is a function of the source position in the field of view as well as of the source spectrum. We have therefore first performed a set of two-temperature fits on the time-resolved spectra, leaving the relative normalization of the LECS and MECS detectors as an additional free parameters. The average value of the MECS to LECS normalization thus determined is 1.15, with a range from 1.03 up to 1.24. The behavior of the fit parameters and of the quality of the fits was then determined by performing the same fits with the relative normalization fixed to the average value of 1.15. A comparison of the probability levels of the two sets of fits shows that leaving the relative normalizations free to vary does not improve the fits, and all the fits discussed in the follow-

Table 1. The spectral parameters derived for the quiescent emission of Algol from the joint analysis of the LECS and MECS spectra, determined on the spectrum accumulated during the time intervals 0, 1 and 18. The fit had a reduced χ^2 of 0.93, with 659 degrees of freedom. For each best-fit parameter the confidence interval is given as computed using the criterion $\Delta\chi^2 = 3.50$, corresponding to the 68% confidence level in the case of three interesting parameters.

T_1 keV	T_2 keV	EM_1 10^{52} cm^{-3}	EM_2 10^{52} cm^{-3}	Z Z_\odot	$N(\text{H})$ 10^{20} cm^{-2}
0.97 [0.89 – 1.1]	3.2 [2.5 – 3.8]	4.1 [3.2 – 5.0]	25. [19. – 31.]	0.37 [0.24 – 0.50]	0.91 [0.54 – 1.3]

ing were thus performed with the relative normalization fixed at 1.15.

All of the spectra discussed here have been fitted with a combination of absorbed thermal emission models. The plasma emission code used has in all cases been the MEKAL model as present in XSPEC, which implements the optically-thin, collisional ionization equilibrium emissivity model described in Mewe et al. (1995). The presence of absorbing material has been accounted for using a WABS component in XSPEC, which implements the Morrison & McCammon (1983) model of X-ray absorption from interstellar material. The metal abundance of the emitting plasma is considered as a free parameter. Abundance values are in the following determined as relative to the “solar” abundance, as determined by Anders & Grevesse (1989). While the global metal abundance was left free to vary, abundance ratios were kept fixed in the fitting process.

3. The quiescent spectrum

Most of the BeppoSAX observation of Algol is occupied by the large flare, and the quiescent emission is visible only in a small time interval, i.e. before the flare itself (during the intervals marked 0 and 1) and during the total phase of the eclipse of the flaring plasma (interval 18). These three spectra have been individually fit with a two-temperature absorbed spectral model with freely varying global metal abundance. Their best-fit parameters are the same within the 1σ confidence range, and they have therefore been summed together in a single spectrum representative of the average “quiescent” emission, from which average spectral parameters have been determined, as listed in Table 1.

Although significantly colder than the flaring emission, the plasma responsible for the “quiescent” emission of Algol still has a high temperature; the 3.2 keV (44 MK) observed here are somewhat higher than the $\simeq 2.5$ keV (29 MK) reported on the basis of ASCA observations by Antunes et al. (1994).

The spectral parameters of the quiescent emission from the ROSAT PSPC observation of Algol (which has a good out-of-flare phase coverage) show the presence of orbital modulation (Ottmann & Schmitt 1996), and thus a proper subtraction of the quiescent emission from the flare spectra would require this effect to be taken into account. Given the very scant phase coverage of the quiescent spectra for the BeppoSAX observation, however, we cannot determine the phase dependence of the spectral parameters of the quiescent emission (if present). The quiescent spectrum has therefore assumed to be constant,

with parameters given by the average of the best-fit parameters of the three quiescent spectra. This average quiescent spectrum has been added as a constant (“frozen”) model component in our subsequent analysis of the flare spectra.

3.1. The H column density

Welsh et al. (1990) report an upper limit, to the H column density toward Algol, of $2.5 \times 10^{18} \text{ cm}^{-2}$ (based on an upper limit to the equivalent width of interstellar Na I lines); Stern et al. (1995) assume (based on these data) a value of $2 \times 10^{18} \text{ cm}^{-2}$ in their analysis of the Algol EUVE spectrum. However, Ottmann & Schmitt (1996) find, from the analysis of the ROSAT PSPC spectra, a value of H column density higher by approximately one dex (1 to $2 \times 10^{19} \text{ cm}^{-2}$). Higher values are found (again from PSPC data) by Singh et al. (1995), who report $3.9 \pm 1.0 \times 10^{19} \text{ cm}^{-2}$, and by Ottmann (1994) who report a range of values (varying with the orbital phase) ranging between 3 and $8 \times 10^{19} \text{ cm}^{-2}$. All X-ray derived values of the absorbing column density are thus significantly higher than the values derived from the EUVE data, and the BeppoSAX quiescent spectrum is no exception, with a 68% confidence range of $5.4\text{--}13 \times 10^{19} \text{ cm}^{-2}$, comparable with the PSPC derived range of values of Ottmann (1994).

Similar discrepancies between the X-ray and EUV-derived H column densities are also observed for other active stars. For example, the H column density toward the RS CVn system AR Lac has been estimated (using the ratio of the 335 and 361 Å Fe XVI lines in the EUVE spectrum) by Griffiths & Jordan (1998) at $\simeq 2 \times 10^{18} \text{ cm}^{-2}$, while Ottmann & Schmitt (1994) derive, from the PSPC spectrum, a value of $\simeq 3 \times 10^{19} \text{ cm}^{-2}$. The value derived from the BeppoSAX spectrum is $\simeq 6 \times 10^{19} \text{ cm}^{-2}$ (Rodonò et al. 1999).

We have tried to fit the quiescent X-ray spectrum with a fixed, low H column density. In practice, any value of $N(\text{H})$ lower than few parts in 10^{19} cm^{-2} results in fits with significantly higher plasma metal abundance than the $1/3 Z_\odot$ obtained by leaving $N(\text{H})$ as a free parameter: to balance the higher soft continuum, the fit process increases the metal abundance, so that the emission from the Fe L complex also increases (see Favata et al. 1997a). As a result, however, the emission from the Fe K complex seen in the MECS detector becomes significantly over-predicted.

To assess the significance of the above discrepancies we have simulated the ability of LECS spectra to determined low values of the H column density and the impact of possible cal-

Table 2. The set of best-fit parameters to the flaring emission, determined through the fitting process described in the text. The first column gives the number of the time interval as plotted in Fig. 2, the second column the time from the beginning of the observation. The last column provides the number of degrees of freedom for each fit. For the best-fit temperature, metal abundance and absorbing column density the confidence interval is given, computed using the criterion $\Delta\chi^2 = 3.50$, corresponding to the 68% confidence level in the case of three interesting parameters. The emission measure is given in units of 10^{54} cm^{-3} .

Int.	t ks	T keV	EM_{54} cm^{-3}	Z Z_{\odot}	$N(\text{H})$ 10^{20} cm^{-2}	χ^2	DOF
2	31.5	12.37 [10.9 – 14.1]	1.83	0.60 [0.46 – 0.76]	26.8 [22. – 32.]	0.927	615
3	40.5	10.96 [10.4 – 11.6]	7.85	1.0 [0.94 – 1.1]	11.0 [10. – 13.]	0.911	615
4	47.0	10.14 [9.8 – 10.5]	11.4	1.1 [1.0 – 1.2]	4.03 [3.8 – 4.6]	1.060	615
5	52.5	8.56 [8.3 – 8.8]	13.3	0.99 [0.94 – 1.0]	1.60 [1.5 – 1.8]	1.293	615
6	58.0	6.76 [6.6 – 7.0]	10.9	0.78 [0.73 – 0.82]	3.32 [3.2 – 3.8]	1.399	615
7	64.0	6.98 [6.8 – 7.2]	8.13	0.66 [0.61 – 0.71]	3.12 [2.9 – 3.6]	1.038	615
8	70.0	7.19 [6.9 – 7.5]	6.83	0.59 [0.53 – 0.65]	1.72 [1.5 – 2.0]	0.998	615
9	76.0	6.72 [6.4 – 7.1]	6.33	0.46 [0.40 – 0.52]	1.23 [0.98 – 1.6]	0.953	615
10	81.5	5.97 [5.7 – 6.3]	5.95	0.45 [0.38 – 0.51]	1.02 [0.72 – 1.4]	0.887	577
11	87.0	5.73 [5.5 – 6.0]	5.65	0.36 [0.30 – 0.43]	1.03 [0.68 – 1.4]	0.87	615
12	97.5	5.37 [5.2 – 5.5]	4.96	0.39 [0.34 – 0.42]	0.852 [0.76 – 1.0]	1.010	615
13	109.0	4.77 [4.6 – 5.0]	4.20	0.36 [0.29 – 0.43]	0.794 [0.61 – 0.99]	0.884	615
14	116.0	4.36 [4.2 – 4.6]	3.79	0.34 [0.26 – 0.42]	0.763 [0.55 – 0.97]	0.863	615
15	124.5	4.27 [4.1 – 4.4]	2.91	0.40 [0.34 – 0.46]	0.620 [0.55 – 0.97]	1.013	615
21	171.0	3.35 [3.2 – 3.6]	1.43	0.26 [0.15 – 0.37]	0.809 [0.50 – 1.8]	0.771	550
22	185.5	2.83 [2.7 – 3.0]	1.00	0.50 [0.35 – 0.65]	1.27 [0.85 – 1.7]	0.826	567

ibration errors on the best-fit column density. Even assuming a perfect calibration, with the S/N of the present spectra column densities of $\lesssim 10^{19} \text{ cm}^{-2}$ cannot be distinguished from zero column densities (although above 10^{19} cm^{-2} their effect becomes visible, see above). The systematics in the LECS calibration are estimated to be at the level of $\lesssim 5\%$, although they could be higher (up to $\simeq 10\%$) in the low-energy (0.1–0.2 keV) range, where the very small absolute area and its steep slope as a function of energy make the calibration very difficult (A. Parmar, private communication). The best-fit column density is very sensitive to possible calibration errors at low-energies: our simulations show that a $\simeq 10\%$ calibration error in the spectral region below 0.2 keV could lead to a systematic bias in the best-fit column density for stellar spectra of few 10^{19} cm^{-2} , comparable with the best-fit column density for the quiescent spectrum. Thus, the absolute value LECS-derived best-fit column densities of this order should be regarded with caution as they critically depend on the calibration being known to better than the currently estimated uncertainty. Relative changes in the absorbing column density (as seen during the flare decay here) would not be affected by such errors, nor would absolute values when the column density becomes considerable ($> 10^{20} \text{ cm}^{-2}$). The influence of such low-energy calibration errors on all other spectral parameters is negligible.

4. Spectral evolution of the flaring emission

For the purpose of determining the time evolution of the spectral parameters of the flaring plasma, the individual time-resolved joint LECS/MECS spectra have been fitted with with a one-temperature absorbed thermal model with freely varying

coronal abundance, plus a two-temperature model with fixed spectral parameters, set to the average values determined for the quiescent spectral emission. The one-temperature model being fit thus represents the flare emission as visible on top of the quiescent spectrum. The resulting best-fit parameters for the flaring component are reported in Table 2.

The temporal evolution of the best-fit temperature, emission measure, abundance and absorbing column density for the flaring component is illustrated in Fig. 4. The one-temperature fits to the flaring plasma emission provide a good description (i.e. a χ^2 value close to 1.0) to most of the spectra, with the exception of the spectra accumulated during the time-intervals 5 and 6, which yield a reduced χ^2 which is formally unacceptable, corresponding to a very low probability level. All other fits yield a reduced χ^2 corresponding to a probability that the adopted model gives a satisfactory description of the data of $\geq 10\%$. We tried to improve the quality of the fit to the spectra accumulated during time intervals 5 and 6 by adding an additional thermal component to the flare spectrum, i.e. assuming that the flare spectrum is better described by a two-temperature model. While the additional degrees of freedom lead to an improved χ^2 for flare spectra 5 and 6 when a two-temperature model is used, the implied probability level for the fit is still very low, and the two-temperature model is still not a good description of the data. In addition, if a two-temperature model is fitted to the flaring spectra for time intervals other than 5 and 6, the resulting spectral parameters are much more poorly determined, with a high degree of degeneracy apparent if the confidence regions are examined.

One obvious feature in the fit residuals for intervals 5 and 6 (which is not altered by the use of a two-temperature

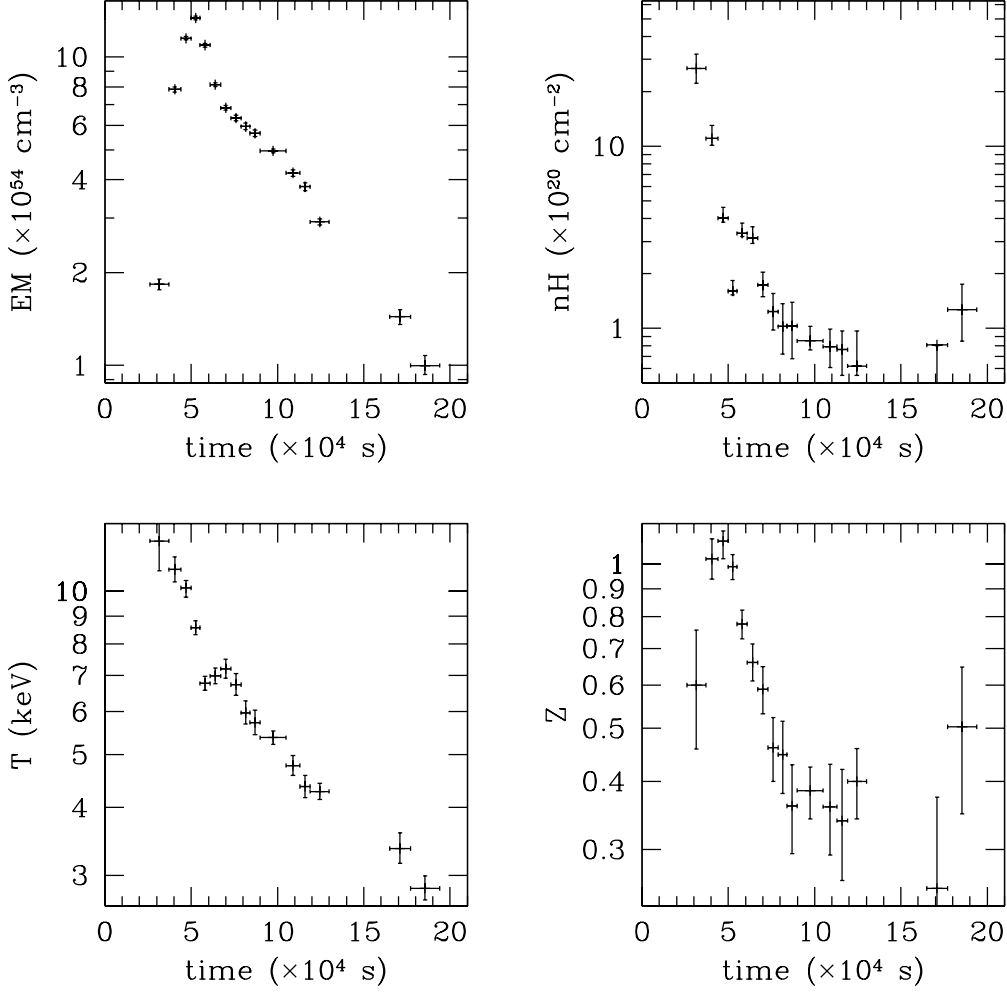


Fig. 4. The time evolution of the best-fit emission measure, temperature, metal abundance and absorbing column density for the best-fit parameters to the one-temperature flare spectra. Time is in seconds since MJD 51 055 03:09:16. The best-fit parameters have been determined from the beginning of the large flare (time interval 2) until the beginning of the second flare visible in the observation (time interval 22). The time intervals affected by the eclipse of the flaring plasma (i.e. from 16 to 20) have also been excluded. The horizontal error bars represent the extent of the time intervals in which individual spectra have been accumulated, while the vertical error bars have been computed using the criterion $\Delta\chi^2 = 3.50$, corresponding to the 68% confidence level in the case of three interesting parameters.

model) is the bump at $\simeq 1.2$ keV. A similar excess in the spectrum is visible, for example, in the ASCA SIS spectrum of Capella discussed by Brickhouse (1998) and Brickhouse et al. (1999), which they attribute to a complex of lines from Fe XVII to Fe XIX from atomic levels with high quantum numbers ($n > 5$). These lines are missing in current models, which will then consistently under-predict the emission in this region, and are likely contributing to the higher χ^2 values found for these time intervals. While one possible way of decreasing the residuals would be to allow selected abundance ratios to vary during the fit, this would not however be granted for the rest of the flare spectra, and doing it only for intervals 5 and 6 would again yield results which cannot be compared with the

rest. Also, as shown by Brickhouse et al. (1999), the lack of the high-excitation Fe lines in the model yields spurious abundances for the other elements if they are left free to vary; we will therefore not explore this possibility further in the present paper.

From Fig. 4 the good temporal coverage of the evolution of the flare is evident, from its onset all the way to its disappearance. Note the gap between $\simeq 130$ and $\simeq 160$ ks due to the eclipse. The general behavior of the flare is similar to the one commonly observed in the several large stellar and solar flares studied so far, with the temperature peaking at the beginning of the flare and the emission measure rising more slowly and peaking at a later time. The shape of the temperature decay

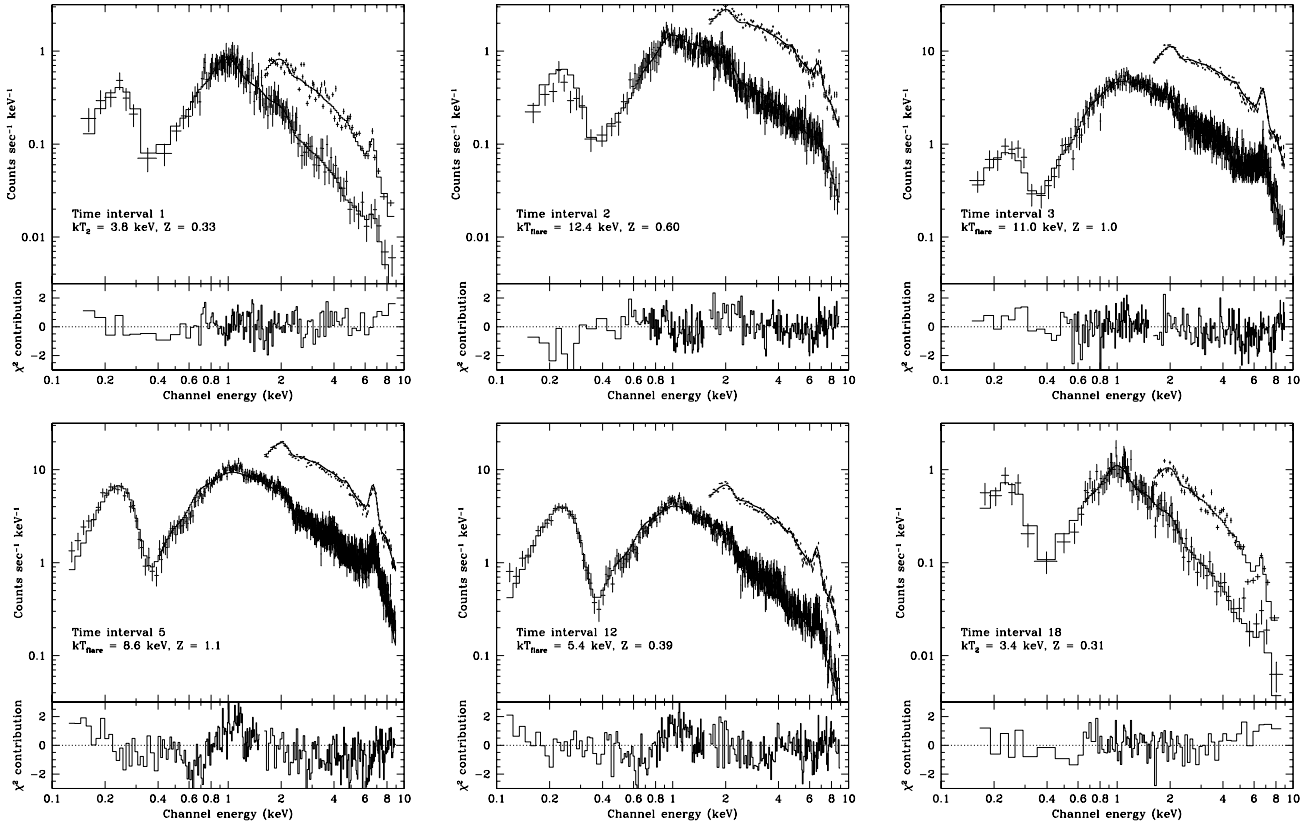


Fig. 5. The LECS and MECS-2 spectra recorded during the time intervals 1, 2, 3, 5, 12 and 18 (as indicated in Fig. 2). The MECS-2 spectra have been shifted upwards by a factor of 5 for clarity. Each plot shows the observed spectra, the best fit model, and, in the lower panel, the (signed) contribution to the χ^2 of each bin. The χ^2 contributions are plotted for the LECS spectrum for $E < 1.6$ keV and for the MECS for $E > 1.6$ keV. The best-fit model plotted is a two-temperature absorbed MEKAL model with varying abundance for intervals 1 and 18, while for the flare spectra (intervals 2, 3, 5 and 12) a one-temperature component with varying abundance has been added on top of the quiescent emission, as described in the text. All the spectra shown have been rebinned at 20 channels per (variable size) bin. Note the change in the vertical scale for the spectra from time segments 3, 5 and 12.

is close to exponential throughout the flare (although it briefly increases again between $\simeq 50$ and $\simeq 70$ ks). The emission measure increases slowly for a long time (~ 20 ks) after the temperature has peaked, and its decay is not well described by a single exponential, with a more rapid decay observable in the first ~ 20 ks of the flare, and a longer decay time-scale observable afterwards, closely mirroring the behavior of the 1.6–10 keV light curve.

4.1. Abundance variations during the flare

As discussed in Sect. 1, previous observations of strong flares on Algol performed with the GINGA and ROSAT observatories hinted at variations of the coronal metal abundance during the flaring event. However, the limited spectral coverage and resolution of the GINGA and ROSAT proportional counters made it difficult to fully disentangle abundance effects from other effects, such as changes in the absorbing column density for the PSPC or changes in the temperature structure in the case

of GINGA. The combination of resolution and spectral coverage of the LECS and MECS detectors allows to effectively disentangle the effects of the plasma metal abundance on the emitted spectrum from the thermal structure (for a discussion see Favata et al. 1997a, b). This, coupled with the excellent time coverage of the BeppoSAX observation and the slow flare decay, allows to study in detail the evolution of the coronal metal abundance during the flare.

The abundance of the quiescent plasma (i.e. the best-fit value of the two-temperature model to the spectra accumulated during the intervals 0, 1 and 18) is $\simeq 0.3$ times the solar photospheric one, a value compatible with the abundance derived for the quiescent Algol corona by Stern et al. (1995) on the basis of an analysis of the EUVE spectrum. The temporal evolution of the best-fit abundance of the flaring plasma is shown in Fig. 4. Consistent with the indications of the ROSAT and GINGA data, the metal abundance of the flaring plasma increases significantly during the early phases of the flare, to a value of approximately 1.0, and then rapidly decays back to

a value consistent with the one determined from the pre-flare spectrum.

The time scale for the increase of the coronal abundance is similar to the time scale with which the emission measure increases, while the abundance “decay” time is significantly faster than either the flare temperature or the emission measure decay times, so that the coronal abundance goes back to its pre-flare value while a significant flaring component is still well visible in the spectrum (with significant excess emission measure and a temperature of some ~ 4 keV). The decaying part of the time evolution of the best-fit abundance is well fit with a single exponential, with an e -folding time of 36 ks, with the further evolution compatible with a constant abundance.

The effect of the varying abundance in the flaring component is clearly visible in the set of spectra plotted in Fig. 5. The pre-flare spectrum (from segment 1) is well fit by a two-temperature plasma with abundance $Z \simeq 0.3$, and a maximum temperature $T \simeq 4$ keV. The spectrum immediately following (from segment 2) marks the beginning of the flare, and shows the presence of the very hot flaring component (with $T \simeq 12$ keV), although still with relatively little emission measure and only a small enhancement (≤ 2 times) in the plasma abundance. In the subsequent spectrum (from segment 3) the temperature has started decaying, while the emission measure is still rising. The plasma abundance has reached its peak at $Z \simeq 1$, so that the Fe K complex is well visible. The spectrum from segment 5 is characteristic of the flare’s emission measure peak. The temperature has decreased to $\simeq 8.6$ keV, while the abundance is still close to the solar value. In the spectrum from segment 12 the emission measure has decayed to less than half the peak value, the flare temperature is down to $\simeq 5.4$ keV and the abundance is back to almost the quiescent value ($\simeq 0.35$), as again evident in the near disappearance of Fe K complex.

Could the changes in the best-fit plasma abundance parameter be explained through mechanisms other than a physical change in the abundance? With the exception of two of the time intervals discussed above, the model used yields fully acceptable reduced χ^2 values, thus making it not necessary to invoke, from a statistical point of view, any other mechanism. For the flare spectra the fit process is driven, in the determination of the abundance, essentially by one diagnostic, i.e. the intensity of the Fe K line complex. For most coronal sources the intensity of the lines in the rich Fe L line complex will be a more important diagnostic of metallicity, given the much higher signal-to-noise ratio and thus statistical weight of the lines in this region of the spectrum, where both the intrinsic photon flux and the instrument’s effective area are higher. However, when the emission is dominated by a plasma at temperatures higher than $\simeq 5$ keV (as in the case of the Algol’s flare spectrum), the spectrum shows very little line emission (specially from Fe L lines), and the only prominent line is the one due to the Fe K complex. Therefore, changing the abundance in the flaring component during the hot phase of the flare leaves the model spectrum essentially unchanged except for the intensity of the Fe K complex.

To show this, we have fit the spectrum from interval 5 with the same type of model (one-temperature on top of the quiescent emission), but excluding from the fit the Fe K region (i.e. channel energies from 5.5 to 8.0 keV) and with the abundance of the flaring component fixed to $Z = 0.4 \times Z_{\odot}$ (i.e. compatible with both the quiescent abundance value and the late-decay flaring value). The resulting best-fit model is shown in Fig. 6, in which the Fe K region has also been plotted. Inspection of the residuals (and their comparison with the relevant panel of Fig. 5) shows that $Z = 0.4 \times Z_{\odot}$ model provides a good fit to all of the spectrum (with the residuals showing the same structure and size as in the case of the $Z \simeq 1.0 Z_{\odot}$ model), but will, as expected, strongly under-predict the Fe K complex. As evident from the size of the residuals at the position of the Fe K complex, they are driving the abundance determination in the flaring emission. Restricting the fit to a higher-energy interval, e.g. to the spectral region harder than 3 keV, does not change the best-fit abundance, although the resulting confidence region are of course broader.

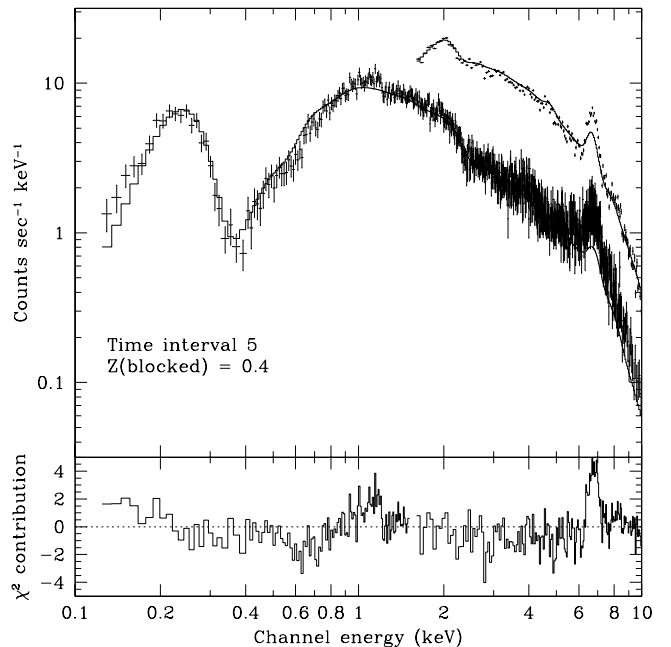


Fig. 6. The spectrum accumulated during interval 5, shown here with a best-fit model for the flaring emission obtained with a single thermal component and a plasma abundance fixed at $Z = 0.4 \times Z_{\odot}$. Channels from 5.5 to 8.0 keV were excluded from the fit, to remove the influence of the Fe K complex emission. They are however plotted here to show the difference in the predicted strength of the Fe K complex.

Fluorescence from the heated photosphere has been proposed as a possible mechanism for the enhancement of the Fe K emission during a strong flare. In this case, however, the emission would come from low ionization states of Fe, and the line

energy would thus be significantly different ($E \simeq 6.4$ keV). At the resolution of the MECS detectors, and at the signal-to-noise ratio of the spectra discussed here, such large shift in energy of the line centroid would easily be seen. We have determined the 90% upper limit to the intensity of a 6.4 keV Fe K line to be $\leq 10^{-3}$ the intensity of the observed 6.8 keV line complex, so that this explanation can be ruled out. The same lack of shift in the line energy allows to rule out significant non-equilibrium ionization effects. Also, the equilibrium time scale for a plasma of this high temperature is of order of few tens of seconds, negligible in comparison with the long time scales on which the abundance is observed to vary.

Given the relative simplicity of the formation mechanism of the Fe K line complex, as well as the absence of other contaminating features in the spectrum, other explanations of the observed strong increase of Fe K emission than an actual abundance increase in the emitting plasma appear rather difficult to find.

4.2. Absorbing material

Inspection of Table 2 shows that the best-fit value for the absorbing column density during the initial phase of the flare is very high ($N(\text{H}) \gtrsim 10^{21} \text{ cm}^{-2}$). This high best-fit absorbing column density is clearly driven by the depressed soft continuum of the initial flare spectra. A comparison of the spectra observed during time intervals 1 (pre-flare) and 2 and 3 (beginning of the flare) as plotted in Fig. 5 shows that while the emission above $\simeq 1$ keV increases considerably once the flare begins, the emission in the region below $\simeq 0.5$ keV is essentially unchanged from its pre-flare values. Given the high temperature of the flaring component ($T \simeq 10$ keV) in this phase (which implies an essentially featureless continuum for the flaring spectrum, with the exception of the Fe K complex emission), the only way to obtain a spectrum significantly depressed in the softer region is by introducing an absorbing column density for the flaring component only. Indeed, inspection of the best-fit model spectrum shows that during time intervals 2 and 3 the flaring spectrum is completely absorbed below $\simeq 0.5$ keV, so that the emission visible is only due to the quiescent component (for which the absorbing column density is fixed). Later during the flare evolution the absorbing column density decreases, so that the soft emission (as visible for time interval 5 in Fig. 5) increases by a factor of $\simeq 10$, to an intensity proportional to the harder part of the spectrum.

The change in absorbing-column density during the flare evolution is also visible in the light curves in the soft (0.1–0.5 keV) and hard (1.6–10.0 keV) band (i.e. Figs. 2 and 3): in the soft band the flare only begins in interval 3, while in the hard band the count rate has already risen by a factor of 10 at the end of interval 2. This apparent “delay” in the flare onset in the softer band can be explained by the high best-fit absorbing column density. The soft-band light-curve also shows a much slower decay than the hard-band one, with an actual rate increase between intervals 6 and 8, and an essentially flat behavior between intervals 8 and 12.

Is the best-fit absorbing column density actually due to real material in the line of sight? An obvious alternative explanation would be that the fit process uses the absorbing column density to compensate for deficiencies in the plasma emission codes. However, given the simplicity of a thermal spectrum at the high temperature observed at the beginning of the flare (dominated by continuum emission) it is hard to imagine that the softer part of the spectrum could be under-predicted by a factor of ten. We thus consider the presence of local absorbing material, depressing the soft emission at the beginning of the flare, to be the correct explanation.

One possible interpretation for this is in terms of a massive coronal mass ejection taking place at the beginning of the flare, which provides the absorbing material.

4.3. The PDS spectra

The PDS detector on-board the BeppoSAX observatory is sensitive to X-rays approximately in the passband from $\simeq 15$ up to $\simeq 300$ keV. Most coronal sources have too little flux in this band to be detected. However, given its very high temperature, the emission from the Algol flare produces an easily detectable signal also in the PDS. We extracted individual PDS spectra from the time intervals 3 to 7 (inclusive), using the tools provided within the SAXDAS package, and jointly fitted the LECS, MECS and PDS data for these intervals, with the same model (a one temperature model superimposed with a two-temperature quiescent emission) which we used for the analysis of the LECS and MECS only. Unfortunately, while it would have been desirable to include the PDS data in the analysis of the time dependence of the flare parameters, the temporal coverage afforded by the PDS data is more limited, and for most of the decay phase no PDS spectra with sufficient signal to noise are available. Thus, to keep the set of parameters for the flare decay homogeneous, we have only used the LECS and MECS data in that context.

The sequence of time-resolved PDS spectra is shown, together with the best-fit model, in Fig. 7. One of the main questions for which the PDS data are of interest is whether any non-thermal spectral components are present in the flare spectrum. The spectra of Fig. 7, together with their residuals, show that the PDS spectrum of flare peak is well described as the high-energy tail of the hot flaring plasma and no additional non-thermal components appear to be present.

All of the PDS spectra present a “bump” in the region close to $\simeq 50$ – 60 keV (particularly visible in the spectrum from interval 4), plus a second minor bump close to 30 keV. Such features are, according to PDS calibration team (D. Dal Fiume, private communication) of instrumental origins, due to a blend of residual lines from the Am calibration source with instrumental fluorescence features due to the Ta collimator (feature at 50–60 keV), while the feature at 30 keV is the escape peak of the feature at higher energy.

The temperature of the flaring component derived from the joint LECS, MECS and PDS fit is, within 1σ , the same as the temperature derived from the LECS and MECS data only, thus

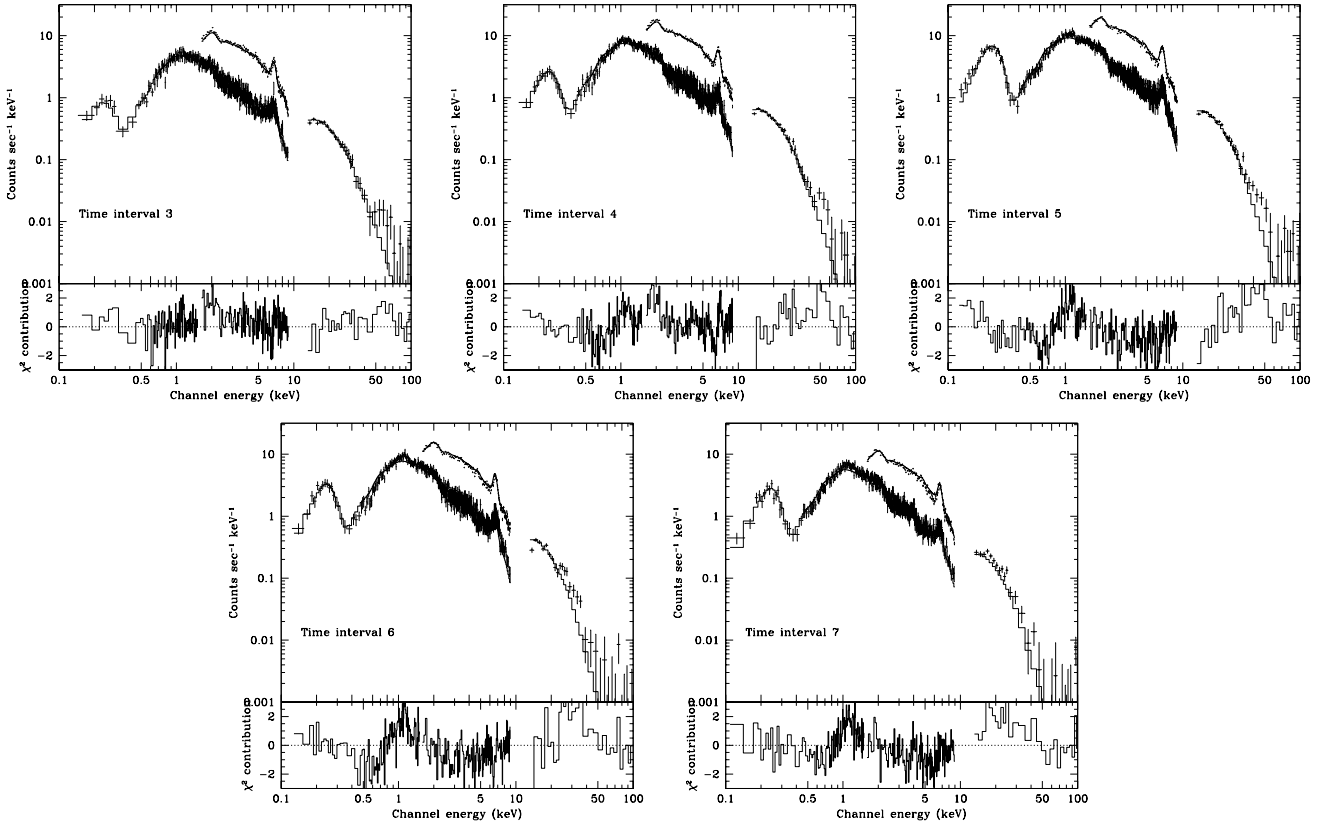


Fig. 7. The LECS, MECS-2 and PDS spectra recorded during the time intervals 3 to 7 (as indicated in Fig. 2). The MECS-2 spectra have been shifted upwards by a factor of 5 for clarity. Each plot shows the observed spectra, the best fit model, and, in the lower panel, the (signed) contribution to the χ^2 of each bin. The χ^2 contributions are plotted for the LECS spectrum for $E < 1.6$ keV, for the MECS for $1.6 \text{ keV} < E < 10$ keV and for the PDS for $13 \text{ keV} < E < 100$ keV. The best-fit model plotted is a one-temperature component with varying abundance on top of a two-temperature absorbed MEKAL model describing the quiescent emission, as described in the text.

confirming that the spectrum seen in the PDS detector is the tail of the thermal spectrum seen in the LECS and MECS pass-bands.

4.4. Energetics

From the detailed temporal evolution of the flare’s spectral parameter it is possible to derive the instantaneous luminosity in the 0.1–10 keV band and therefore, by integration, the total energy emitted in soft X-rays during the flare. The temporal evolution of the X-ray luminosity is shown in Fig. 8.

The total X-ray radiative loss at the end of the flare is 1.4×10^{37} erg, making this one of the most energetic X-ray flares ever observed on stellar sources, on a par with the long flare observed on CF Tuc by Kürster & Schmitt (1996).

Given the short thermodynamic decay time of the loop implied by the eclipse-derived size ($\lesssim 10$ ks, see Sect. 6), the loop has, on the total time scale of the flare, negligible thermal inertia, i.e. it will quickly respond to changes in the heating. Thus, the observed X-ray luminosity temporal evolution closely describes the temporal evolution of the heating, slowly rising for

some tens of ks and then decaying for more than 100 ks. Whatever the mechanism ultimately responsible for the heating is, it thus must be capable of operating on these time scales.

5. Analysis of the flare decay

Different approaches have been proposed to determine, from the temporal evolution of the flare temperature and emission measure, the parameters, and in particular the size (and thus density) of the flaring region. One unique feature of the Algol flare discussed here is the availability of an actual measurement of the physical size of the flaring region from the duration and shape of its eclipse (Schmitt & Favata 1999). Thus, for the first time we can test whether the different methods used to analyze the flare decay phase yield answers consistent with the size of the flaring region implied by the eclipse.

5.1. Assumptions

All the methods discussed in the literature rely on the analysis of the decay phase of the flare, defined as the phase of the

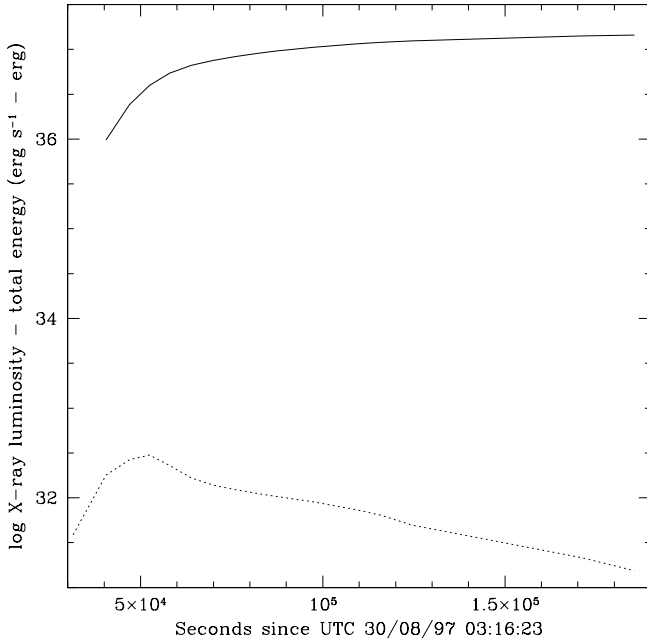


Fig. 8. The evolution of the flare’s X-ray luminosity in the 0.1–10 keV band (lower curve) together with the total X-ray emitted energy in the same band (higher curve).

flare during which both the temperature and the total number of emitting particles (using the emission measure, or more properly its square root, as proxy) decrease. This is equivalent to saying that the total energy content of the flaring loop is decreasing.

5.2. The quasi-static cooling formalism

In this Section we follow the quasi-static formalism for the analysis of the decay phase of a flare, as developed by van den Oord & Mewe (1989) and as applied, for example, to the analysis of the large PSPC flare on Algol by Ottmann & Schmitt (1996). In this framework the information about the linear size of the flaring loop is derived from the observed relaxation times of the cooling plasma, under the assumption that the two relevant mechanisms for energy loss from the flaring plasma are radiation and thermal conduction along the loop. The ratio between the conductive and radiative time scales (τ_c/τ_r) is in general unknown, given that τ_c will depend on the geometry of the flaring loop(s). The quasi-static formalism requires this ratio to be constant. Under this condition the geometry of the loop can then be determined.

Following van den Oord et al. (1988), the effective decay time for the thermal energy during the loop decay is defined as

$$\frac{1}{\tau_{\text{eff}}} = \frac{1}{\tau_r} + \frac{1}{\tau_c} = \frac{(1 + \gamma/2)}{\tau_T} + \frac{1}{2\tau_d} \quad (1)$$

where τ_T is the decay time of the loop temperature, τ_d is the decay time of the light-curve and γ is the power law exponent

of the temperature dependence of the radiative cooling function Ψ of an optically thin plasma hot plasma. This function is usually parameterized as $\Psi(T) = \Psi_0 T^{-\gamma}$, and for sufficiently hot plasmas ($T \gtrsim 20$ MK) the values $\Psi_0 = 10^{-24.73}$ and $\gamma \simeq -0.25$ provide a very good parameterization of the radiative cooling losses. Note that at these temperatures the emission is dominated by the continuum, with very little line contribution, and hence the emissivity does not depend on the metal abundance, making this approach applicable even in the presence of observed abundance variations.

The radiative and conductive decay times are defined as

$$\tau_r = \frac{3n_0 k_B T_0}{n_0^2 \Psi_0 T_0^\gamma} \quad (2)$$

and

$$\tau_c = \frac{3n_0 k_B T_0}{8\kappa_0 T_0^{7/2} f(\Gamma)(\Gamma + 1)L^2} \quad (3)$$

where n_0 and T_0 are the electron density and the temperature at the beginning of the decay phase and L and Γ are the length and expansion factor of the loop. $f(\Gamma)$ is a correction factor accounting for the change in the conductive flux for tapered loops. The adopted value for the conductivity is $\kappa_0 = 8.8 \times 10^{-7} \text{ erg cm}^{-1} \text{ K}^{-7/2}$.

To determine whether the quasi-static formalism is applicable in principle, the constancy of the ratio between the radiative and conductive cooling time during the flare decay has to be checked. This ratio can be written as (Eq. (27) of van den Oord & Mewe 1989):

$$\mu = \frac{\tau_r}{\tau_c} = C \times \frac{T^{13/4}}{EM}, \quad (4)$$

where C is a constant incorporating all the geometrical factors and the subscripts to T and EM indicate the power of 10 which the relevant quantity has been normalized to (in cgs units). In a quasi-static cooling phase this quantity must be constant. The time evolution of μ for the Algol flare discussed here is plotted in Fig. 9, using the values of T and EM shown in Fig. 4. Once the emission measure has reached its peak (i.e. in time interval 5) μ is constant within the error bars, although with some evidence for a slight increase between time intervals 6 to 8, which may indicate additional heating, as observed in the time evolution of the plasma temperature (see Fig. 4).

5.2.1. The shape of the decay

The formalism discussed above implicitly assumes that a decay time can be uniquely defined, i.e. that the relevant quantities decay in a smooth and monotonic way. For the flare discussed here it is evident that the decay phase encompasses different phases: a first phase (intervals 4–5) in which the light curve as well as the derived temperature and emission measure are decaying exponentially on a rather fast e -folding time scale, a phase in which the decay has slowed down and in which the temperature is increasing again (intervals 6–8, obviously indicative of the presence of prolonged heating) and a final long

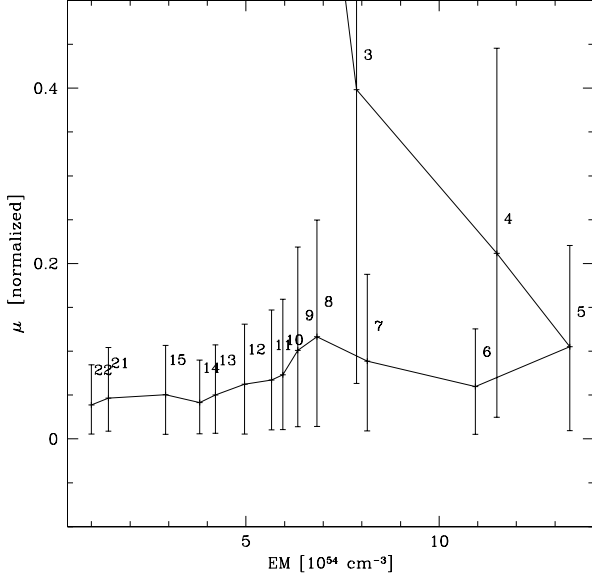


Fig. 9. The temporal evolution of the μ parameter (the ratio between the radiative and conductive cooling time for the loop in quasi-static formalism) during the flare.

decay phase in which the light curve decay is well described by a slow exponential decay, similar to the temperature and emission measure decays. Thus, the conditions for the quasi-static formalism are not satisfied for the whole decay phase; however, it should be applicable to the phase in which the decay is monotonic and smooth, with an exponential light curve, i.e. between time intervals 8 and 14 inclusive.

During this interval the e -folding times for the temperature and count rate of the flare are 97 and 64 ks respectively, which combine to yield an effective decay time, as defined above, $\tau_{\text{eff}} = 59$ ks. The temperature at the beginning of the decay phase thus defined is 7.2 keV, or 83 MK, and the emission measure is $6.4 \times 10^{53} \text{ cm}^{-3}$. If we apply the formalism of van den Oord & Mewe (1989), we can calculate the size of the flaring loop as a function of the loop expansion factor Γ , and of the number N and the ratio α between the loop's length and its diameter at the base. The resulting relationship between the loop length and $N\alpha^2$ is plotted in Fig. 10. Unless very small loop diameters are postulated (i.e. smaller than one hundredth of the loop length), Fig. 10 shows that the flaring loop must be longer than a few times 10^{12} cm (i.e. of order 10 stellar radii), independent from any possible loop expansion.

5.2.2. Scaling law approximation

To further constrain the geometry of the flaring loops, we can follow the approach of Stern et al. (1992), who show that, once the applicability of the quasi-static framework has been verified, the geometric parameters of the flaring loops, as well as the plasma density, can be derived through simple scaling laws from the detailed analysis of van den Oord & Mewe (1989) of

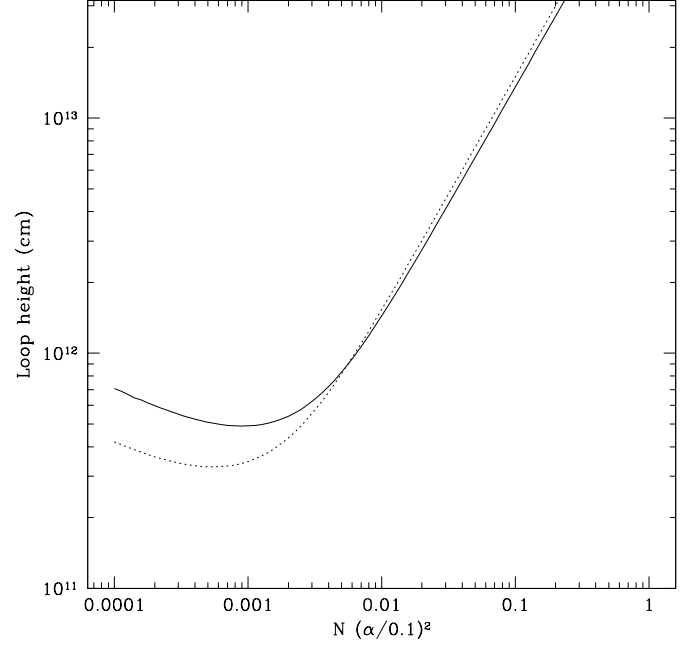


Fig. 10. The loop's length calculated in the framework of the quasi-static cooling formalism, as a function of the quantity $N(\alpha/0.1)^2$, where N is the number of flaring loops and α is the ratio between the loop's length and its diameter. The dashed curve is for loops with a rather strong expansion ($\Gamma = 10$), while the continuous curve is for a loops without any expansion ($\Gamma = 1$).

the EXOSAT flare of Algol (their Eqs. (19)). The constancy of the ratio between the radiative and conductive cooling time gives a scaling law of the form

$$n_A L \propto T_A^{(2\gamma+7)/4} \quad (5)$$

where the subscript A refers to the apex of the loop, where the bulk of the emitting plasma is located. Combining the above equation with the definition of the radiative cooling time τ_r (Eq. (2)), yields $L \propto \tau_r^{7/8}$ (again for $\gamma = -0.25$), and $n \propto \tau_r^{-1} T^{6/8}$. If we scale from the analysis of van den Oord & Mewe (1989), the decay time of the flare observed here is 10.5 times longer, while the temperature at the beginning of the decay phase is 1.44 times higher. Thus, the loop length is 14.5 times longer, or 2.3×10^{12} cm, and the density is 8.0 times lower, or $3.3 \times 10^{10} \text{ cm}^{-3}$. The remaining geometrical parameters for the flaring loops can be derived from the definition of the emission measure

$$EM \simeq \frac{\pi}{8} n_e^2 L^3 (\Gamma + 1) N \alpha^2 \quad (6)$$

where the relationship is approximate because of the (weak) dependence of the scaling laws on Γ . Substituting all the values yields $(\Gamma + 1)N(\alpha/0.1)^2 = 1.2 \times 10^{-2}$.

The loop length predicted by the quasi-static formalism for the flare discussed here is clearly substantial: a length of

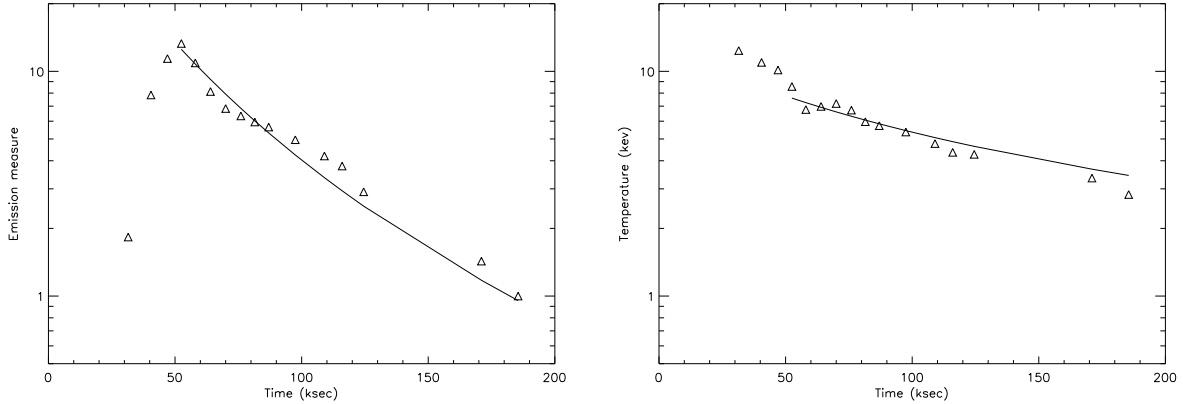


Fig. 11. The best-fit decay curves for the emission measure (left panel) and temperature (right panel) during the flare’s decay, obtained with a full fit to the quasi-static formalism of van den Oord & Mewe (1989), considering the complete decay of the flare. The emission measure is plotted in units of 10^{54} cm^{-3}

$2.3 \times 10^{12} \text{ cm}$ corresponds to a loop height of $1.4 \times 10^{12} \text{ cm}$, or $5.7 R_K$, large but still within the pressure scale height for the K star in Algol (for the hot plasma at the beginning of the decay phase – 83 MK – the pressure scale height for the K star is $\simeq 6 \times 10^{12} \text{ cm}$, or $24 R_K$).

If the decay time constants are derived from the complete decay phase, i.e. from the moment in which both T and EM start to decrease (interval 5) the results do not change significantly. In this case the precise form of the decay is ignored, and only the time scales are considered. This approach is also likely to be more consistent with the majority of the published results on stellar flares, in which neither the temporal coverage nor the statistics are sufficient to show the details of the time evolution of the flare parameters, and a single determination of the decay time constants starting from the flare peak is done. For example, for the Algol flare observed by ROSAT, only a sporadic coverage of the flare light curve was available, so that any short-lasting intermediate heating episodes such as the ones evident in this case would not have been detected.

In the present case the e -folding times (derived from the peak of the quantity of interest) for the temperature and count rate are, respectively, 118 and 59 ks, combining to yield an effective decay time of 63 ks, and the temperature at the beginning of the decay is 98 MK. Application of the same scaling laws as above results in a loop length of $2.8 \times 10^{12} \text{ cm}$ and a plasma density of $3.5 \times 10^{10} \text{ cm}^{-3}$, essentially identical to the results obtained by considering only the exponential part of the decay.

5.2.3. Full fits to the scaling-law formalism

We have also performed a full fit of the equations of van den Oord & Mewe (1989) to the complete decay phases of the temperature and count rate. The resulting best-fit is shown in Fig. 11. The resulting loop length is $1.7 \times 10^{12} \text{ cm}$ with a corresponding plasma density of $\simeq 10^{10} \text{ cm}^{-3}$. Again, the resulting

loop length and density are quite similar to the value obtained with a simple application of the scaling laws to the exponentially decaying part of the light curve, confirming the relative insensitivity of the quasi-static formalism to the details of the starting assumptions.

5.3. The slope in the temperature-density diagram

A different approach to the analysis of the decay times of spatially unresolved flares has been developed by Reale et al. (1997). This method simultaneously yields estimates for the physical size of the flaring loop as well as for the presence and time scale of heating during the decay phase of the flare. The method uses the slope of the locus of points in the temperature versus density diagram during the flare decay phase (Sylwester et al. 1993) as a diagnostic of the presence of sustained heating. Under the assumption that the loop volume remains constant during the flare, the square root of the emission measure is used as a proxy for the density; we will refer to this approach, in the following, as the EM vs. T slope method.

Detailed hydrodynamical simulations show that flares decay approximately along a straight line in the $\log \sqrt{EM} - \log T$ diagram, and that the value of the slope ζ of the decay path is related to the ratio between the observed decay time of the light curve τ_c and the “natural” thermodynamic cooling time of the loop without additional heating τ_{th} . The validity of the simulation-derived relationship has then been verified by Reale et al. (1997) with a sample of solar flares observed by Yohkoh. This approach allows to explicitly estimate the intrinsic spread of the derived physical parameters; in practice the estimated loop size agrees, for the solar case, to $\simeq 20\%$ with the actual size. The recalibration of the method for temperatures and emission measures derived with the BeppoSAX MECS detector is discussed by (Pallavicini et al. in preparation).

In practice, an observed flare decay with a slope $\zeta \simeq 1.7$ (again for T and EM derived with the MECS detector) implies that no additional heating is present ($\tau_h = 0$) while smaller values of ζ imply progressively longer heating time scales. The relationship between ζ and τ_{lc}/τ_{th} becomes effectively degenerate at values of ζ smaller than about 0.4, so that $\zeta \lesssim 0.4$ implies a heating time scale comparable to the observed decay time of the flare (see Fig. 2 of Reale et al. 1997). The loop size is estimated as a function of τ_{lc} , T_{max} and ζ (where T_{max} is the peak flare temperature, not the temperature at the beginning of the decay phase). For a given τ_{lc} and T_{max} , the smaller ζ (and thus the longer the additional heating) the smaller the implied loop length. In a large fraction of the solar flares examined by Reale et al. (1997) significant heating is present, so that the thermodynamic decay time of the loop alone significantly over-estimates its size (by factors between 2 and 10).

The evolution of the spectral parameters for the Algol flare is plotted, in the $\log \sqrt{EM} - \log T$ plane, in Fig. 12. The set of \sqrt{EM} , $\log T$ pairs plotted includes the rising phase of the flare (up to interval 5), when the emission measure is still building up, and thus the decay has not yet begun. Afterwards the initial very steep decay only lasts for a relatively brief time, as the temperature increases again in intervals 6 to 8. The apparently undisturbed decay begins, as discussed in the framework of the quasi-static method, with interval 8, and, up to interval 14, follows a clean straight line. The last three intervals (which however do not sample very well the light curve, being interrupted by the eclipse) show evidence for a change in the slope, which becomes shallower.

Reale et al. (1997) quote four conditions for the method to yield optimal results, i.e. the slope ζ must be greater than 0.3, the light curve must decay exponentially, the trajectory of the decay in the $\log T - \log \sqrt{EM}$ plane must be linear and the resulting loop length must well below the local pressure scale height. In the present case the decay is indeed not linear, but there is clear evidence for an episode of reheating, so that the slope ζ is not very well constrained, and the resulting uncertainties are likely to be significantly larger. The choice of which interval of the observed decay to use for the determination of the flare parameters is, in this case, prescribed by the method; it begins when the emission measure peaks and ends with the time interval in which the light curve has decayed to a count rate of 10% of the peak value.

The average slope of the decay in the $\log T - \log \sqrt{EM}$ plane is 0.84 ± 0.20 (90% uncertainty, as in all of the following). By applying the equivalent of Eq. (3) of Reale et al. (1997), the ratio between the observed light-curve decay time and the thermodynamic decay time of the flaring loop (i.e. the decay time which would be observed in the absence of heating) is given by (recalibrated for the BeppoSAX MECS detector)

$$\tau_{LC}/\tau_{th} = 8.68 \times e^{-\zeta/0.59} + 0.3 = F(\zeta) \quad (7)$$

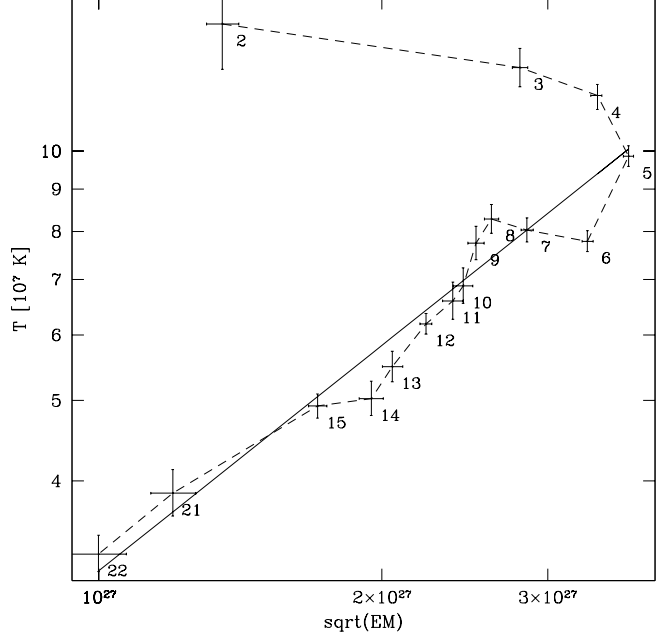


Fig. 12. The evolution of the flare temperature (in K) and square root of the emission measure (in cm^{-3} , a proxy to the plasma density, in the assumption of a constant volume). The error bars are 1σ for three interesting parameters ($\Delta\chi = 3.50$), and the dashed line connects each individual point, to guide the eye. Also indicated is the correspondence with the time intervals defined in Fig. 2. The continuous line is the fit to the points from 8 to 22.

In our case, $\tau_{LC}/\tau_{th} = 2.4$. The loop length is given by the equivalent of Eq. (4) of Reale et al. (1997), i.e.

$$L = \frac{\tau_{th} \sqrt{0.233 \times T_p^{1.099}}}{3.7 \times 10^{-4}} \quad (8)$$

where T_p is the measured peak flare temperature. Substituting the values determined for the Algol flare, i.e. $\tau_{LC} = 49.6 \pm 4.5$ ks (determined from the peak down to the 10% level), $\tau_{th} = 20.1$ ks, $T_p = 138$ MK, the predicted loop length is $L = 8.2 \times 10^{11}$ cm ($3.3 R_K$), with a 90% uncertainty on the derived length is $\pm 3.5 \times 10^{11}$ cm, yielding a formally allowed range of loop lengths of 4.7 to 11.7×10^{11} cm, i.e. 1.9 to $4.7 R_K$. The peak temperature at the loop apex is $T_{max} = 200$ MK. As expected for a flare with significant heating, the loop length derived is significantly shorter (a factor of 2 to 4) than the value derived through the quasi-static formalism under the assumption of no heating.

No density estimate is produced directly by the EM vs. T slope analysis. A simple-minded estimate can be derived by computing the loop's volume (with a given assumed value of α , typically $\simeq 0.1$) and computing

the peak density from the peak emission measure through the simple relationship

$$n \simeq \sqrt{\frac{EM}{V}} \simeq \sqrt{\frac{EM}{2\pi\alpha^2 L^3}} \quad (9)$$

The density corresponding to the range of loop lengths derived through the EM vs. T slope method is $2.7 \times 10^9/\alpha$ to $1.9 \times 10^9/\alpha \text{ cm}^{-3}$.

6. Comparison with the flaring region size determined by eclipse analysis

The lengths derived through the analysis of the flare decay range between 4.7×10^{11} cm (the lower end of the range of values allowed by the EM vs. T slope method) and 28×10^{11} cm (the longer value obtained with the quasi-static formalism); the corresponding loop heights (under the assumption of a simple, single-loop geometry) above the stellar surface range from $\simeq 1.2$ to $\simeq 7$ radii of the K star. The corresponding plasma densities are few times $\simeq 10^{10} \text{ cm}^{-3}$.

How realistic are the long tenuous loops implied by the quasi-static decay-phase analysis? Unlike any previous stellar flare, we can in this case compare these values with the allowed volume for the flaring plasma derived from a geometrical analysis of the eclipse of the X-ray emission. As discussed in detail in Schmitt & Favata (1999), the observed total eclipse of the flaring plasma implies a maximum height of the flaring region of less than $\simeq 0.6$ stellar radii, i.e. $h \leq 0.6 R_K \simeq 1.5 \times 10^{11}$ cm, equivalent to a maximum loop length (assuming a vertical loop with a simple geometry) of $\leq 2.4 \times 10^{11}$ cm, significantly smaller than the values derived by the analysis of the quasi-static flare decay. The lower end of the allowed range for the loop lengths derived with the EM vs. T slope method is closer to the geometrical size derived through the eclipse analysis, but still marginally too large.

An immediate consequence of the small volume implied by the eclipse is that the flaring plasma must have a higher density than predicted by the quasi-static analysis. The density is estimated by Schmitt & Favata (1999) at $f^{-0.5} \times 10^{11} \text{ cm}^{-3}$, where f is the filling factor for the flaring plasma within the region allowed by the eclipse, $f < 1$. The high density in turn implies a decay time for radiative cooling for the plasma of $24f^{0.5}$ ks, and a conductive decay time only $2.5f^{-0.5}$ ks, with a resulting effective decay time, for any value of f , negligible when compared with the observed long decay time of the flare. Therefore, the observed decay must be driven almost entirely by the evolution of the energy dissipation responsible for the heating. In this framework, the observed irregularity of the observed flare decay is then not so much related to details of the decay process or of the flaring structure, but rather to the temporal evolution of the energy dissipation process.

The large loop sizes derived from the quasi-static analysis of flare decay, although somewhat extreme, are not unusual: large loop lengths are a common result from the decay-phase analysis of large flares observed on all classes of coronal sources. For example, Schmitt (1994) shows that, using the

quasi-static cooling paradigm, for the flare on the dMe star EV Lac observed during the ROSAT All Sky Survey the implied loop length is 6×10^{11} cm (i.e. $\simeq 10$ stellar radii); recently, Tsuboi et al. (1998) reported the detection of a large flare on the pre-main sequence star V773 Tau, showing that the observed cooling time implies loop sizes of $\simeq 4 \times 10^{11}$ cm, or $\simeq 1.2$ stellar radii; the very long ROSAT flare observed on the active binary CF Tuc (Kürster & Schmitt 1996) implies (depending on the details of the assumptions) loop lengths of order 2 to 5×10^{11} cm, again comparable to or larger than the stellar radius. Such large loop sizes are in contrast with the solar case, where, even for the strongest flares, the size of the flaring loops remains well below the solar radius. While the energy released for the stellar flares discussed here is several orders of magnitude larger than in the case of the strongest solar flares, and thus the solar analogy may not necessarily be fully relevant, the very large loops raise several difficulties related to the high implied magnetic fields at large distances from the stars, the heating mechanisms, etc. While the presence of long magnetic structures anchored on both stars could somewhat alleviate these concerns in the case of active binary systems (but not for Algol-type systems), this would not work in the case of single stars.

Thus the physical meaning of the long loop sizes derived for spatially unresolved stellar flares from the quasi-static analysis of the loop decay appears questionable when compared with the geometric constraints on the size of the flaring region derived from the eclipse analysis. The present observations show that large flares can be produced by quite compact, high density structures, much smaller than implied by the quasi-static analysis of the loop decay phase or by simple considerations about the radiative decay time of an undisturbed plasma. Sustained heating, fully dominating the observed decay, must therefore, in such cases, be present. The heating mechanism must then not be impulsive only, but must be followed by a long-lasting tail, with time scales of order of tens of ks. The EM vs. T slope analysis in this case does not yield a very stringent limit to the size of the flaring loop (and it still appears to marginally overestimate the loop's size), but provides clear support for the presence of long-lasting heating.

The applications of the EM vs. T slope analysis in a situation in which the flare decay in the $\log T - \log \sqrt{EM}$ plane is not linear is likely to result in larger uncertainties on the derived parameters. The flare shows clear evidence for a significant reheating episode (in time intervals 6 to 8), which alters the decay path, unlikely the hydrodynamic simulations which are used to derive the loop's size, in which the heating is parameterized as a monotonically decreasing function of time. Note that if the same flare had been observed at a significantly lower S/N , such reheating episode would not have been resolved, but it would simply have resulted in a linear but shallower flare decay, biasing the resulting flare parameters. One alternative possibility is that the flare is the result of a different physical process that the single, constant-volume loop (a "compact" flare) which is assumed throughout the analysis. This could be, e.g. – similarly to the solar "two-ribbon" flares – an evolving

loop arcade. Once more this would imply that different physical conditions compared to the hydrodynamic simulations of Reale et al. (1997), and thus larger uncertainties on the results.

6.1. Comparison with previous flares observed on Algol

A few major flares have already been observed on Algol by a variety of X-ray telescopes. The physical parameters derived from the analysis of the decay phase are listed in Table 3.

Table 3. A comparison of the physical parameters derived for different flares on Algol from the GINGA, EXOSAT and ROSAT flares. The first column gives the maximum temperature measured in the flare, the second column the temperature at the beginning of the decay phase, the third column the maximum emission measure measured during the flare. The fourth column gives the effective decay time for the flare, while the remaining two columns give the plasma density and the loop length derived from the quasi-static analysis. Numerical subscripts indicate the power of 10 by which the relevant quantity has been scaled.

Instr.	T_p MK	T_d MK	EM_{54} cm^{-3}	τ_{eff} ks	n_9 cm^{-3}	L_{10} cm
GINGA	67	65	1.34	22.5	50	60
EXOSAT	80	58	0.98	5.2	260	16
ROSAT	88	39	10.0	15.4	170	12

Table 4. A comparison of the physical parameters derived for the BeppoSAX flare of Algol, derived using different methods and assumptions. “QS-SL-EX” indicates application of the quasi-static formalism to the exponentially decaying part of the light curve, and using the scaling laws of Stern et al. (1992) to obtain the loop parameters; “QS-SL-FD” indicates the same approach applied to the full decay phase; “QS-FF-FD” indicates application of the quasi-static approach, with a full-fit of the complete decay phase to the equations of van den Oord & Mewe (1989); “R+97-FD” indicates application of the Reale et al. (1997) formalism to the complete decay phase, while the row marked with “Eclipse” indicates the parameters derived from the analysis of the eclipse light curve by Schmitt & Favata (1999). In this last case only the loop length and density are derived; the density includes the unknown filling factor f . Numerical subscripts indicate the power of 10 by which the relevant quantity has been scaled.

Method	T_p MK	T_d MK	EM_{54} cm^{-3}	τ_{eff} ks	n_9 cm^{-3}	L_{10} cm
QS-SL-EX	140	83	13.3	59.0	33	230
QS-SL-FD	140	98	13.3	63.0	35	280
QS-FF-FD	140	90	13.4	43.5	90	174
R+97-FD	140	140	13.3	22.6	$\simeq 2/\alpha$	47–120
Eclipse	140	–	–	13.3	$94/\sqrt{f}$	24

For comparison we also list, in Table 4, the parameter values derived, for the BeppoSAX flare, with the different approaches discussed above.

7. Conclusions

The large Algol flare discussed here has several unique characteristics, already listed in the Introduction, which make it a unique event given the level of detailed constraints which can be derived on the flaring process. The most important conclusions are:

- The variations of metallicity of the flaring plasma (which had already been hinted at in the study of previous X-ray flares) can be unambiguously determined. The long duration of the flare and the good count statistics make it possible to determine the temporal evolution of the metal abundance, showing that it rises by a factor of three during the flare rise and decays again to the pre-flare value on time scales faster than any of the observed time scales (for the light curve, emission measure of temperature decay). Alternative explanations (as opposed to real abundance variation effects) for the observed changes in the spectrum, such as non-equilibrium effects, are difficult to reconcile with the plasma density for the flaring loop (a fortiori for the higher densities implied by the eclipse), which imply that the plasma would relax to equilibrium ionization conditions in a few tens of seconds at most. Fluorescence from the X-ray bombarded photosphere is in contrast with the lack of observed shift of the centroid of the Fe K line toward 6.4 keV and from the fact that the flare occurs in the permanently-occulted pole of the K-type star, so that the potentially fluorescing photosphere would in any case be largely self-eclipsed.
- During the initial (rising) phase of the flare the best-fit absorbing column density is large ($\simeq 3 \times 10^{21} \text{ cm}^{-2}$), and decays on time scales of some tens of ks. We interpret this as possibly associated with moving, cool absorbing material in the line of sight, i.e. a major coronal mass ejection associated with the flare’s onset.
- The length derived for the flaring loop from the analysis of the flare decay, with the quasi-static formalism of van den Oord & Mewe (1989) is consistently too large when compared with the upper limit on the size of the flaring region imposed by the observed total eclipse (see Schmitt & Favata 1999). Different assumptions result in a small range of derived loop half-lengths (from 18 to $28 \times 10^{11} \text{ cm}$), they are all well above the eclipse-derived upper limit of $2.4 \times 10^{11} \text{ cm}$. Given the nature of the geometric constraints imposed by the eclipse observations, the conclusions is thus that the decay-derived loop lengths are too large, by a factor of at least a few times, and the derived densities are correspondingly lower. This may be relevant also for the interpretation of the very large loop sizes which have been determined with this method in the past for other large X-ray flares on other stars.

- The range of loop lengths derived with the analysis method of Reale et al. (1997) imply the presence of significant sustained heating, in agreement with the conclusions drawn on the basis of the eclipse-derived size. The derived lengths are still marginally too large with respect to the eclipse-derived size; this is likely due to the application of the method in the presence of a significant reheating episode, which (when compared with hydrodynamical simulations with monotonically decreasing heating) will introduce additional uncertainties in the results. Nevertheless, even in such case, this method appears to yield more reliable information on the physical conditions of the flaring region than the quasi-static method.
- As a consequence of the smaller loop length implied by the eclipse, sustained heating must be present throughout the flare, and it must actually be driving the decay. Given the small intrinsic thermodynamic decay time of the loop implied by the small size and corresponding high density, the loop has a small “thermal inertia”, and thus the heating time profile must essentially be the same as the observed X-ray luminosity profile (given in Fig. 8).

Acknowledgements. We would like to thank M. Guainazzi and D. Dal Fiume for their help in the analysis and understanding of the PDS data, and A. Parmar for the useful discussion on the LECS data. We are grateful to F. Reale for the several illuminating discussions on his methodology for the analysis of flare decays as well as for calibrating his method for the BeppoSAX MECS detectors. The BeppoSAX satellite is a joint Italian and Dutch program.

References

- Al-Naimiy H. M. K., Mutter A. A. A., Flaih H. A. 1985, *Ap&SS* 108, 227
- Anders E., Grevesse N. 1989, *Geochim. Cosmochim. Acta* 53, 157
- Antunes A., Nagase F., White N. E. 1994, *ApJ* 436, L83
- Boella G., Butler R. C., Perola G. C. et al. 1997a, *A&AS* 122, 299
- Boella G., Chiappetti L., Conti G. et al. 1997b, *A&AS* 122, 341
- Brickhouse N. S. 1998, in R. Donahue, J. Bookbinder (eds.), 10th Cambridge Workshop on Cool Stars, Stellar Systems and the Sun, Vol. 154 of ASP Conf. Series, ASP, San Francisco, p. 487
- Brickhouse N. S., Dupree A. K., Edgar R. J. et al. 1999, *ApJ* submitted
- ESA 1997, *The Hipparcos and Tycho catalogues*, Vol. 1 of *SP-1200*, ESA, Noordwijk
- Favata F., Maggio A., Peres G., Sciortino S. 1997a, *A&A* 326, 1013
- Favata F., Maggio A., Peres G., Sciortino S. 1997b, in R. Donahue, J. Bookbinder (eds.), 10th Cambridge Workshop on Cool Stars, Stellar Systems and the Sun, Vol. 154 of ASP Conf. Series, ASP, San Francisco, 1027
- Frontera F., Costa E., Dal Fiume D. et al. 1997, *A&AS*, 122, 371
- Gehrels N. 1986, *ApJ* 303, 336
- Griffiths N. W., Jordan C. 1998, *ApJ* 497, 883
- Harnden F. R. J., Fabricant D., Topka K. et al. 1976, *ApJ* 214, 418
- Hill G., Barnes J. V., Hutchings J. B., Pearce J. A. 1971, *ApJ* 168, 443
- Kim H.-I. 1989, *ApJ* 342, 1061
- Kopp R. A., Poletto G. 1984, *Sol. Phys.*, 93, 351
- Kürster M., Schmitt J. H. M. M. 1996, *A&A* 311, 211
- Mewe R., Kaastra J. S., Liedahl D. A. 1995, *Legacy*, 6, 16
- Morrison R., McCammon D. 1983, *ApJ* 270, 119
- Ottmann R. 1994, *A&A* 286, L27
- Ottmann R., Schmitt J. H. M. M. 1994, *A&A* 283, 871
- Ottmann R., Schmitt J. H. M. M. 1996, *A&A* 307, 813
- Pallavicini R., Tagliaferri G., Stella L. 1990, *A&A* 228, 403
- Parmar A. N., Martin D. D. E., Bavdaz M. et al. 1997, *A&AS*, 122, 309
- Reale F., Betta R., Peres G., Serio S., McTiernan J. 1997, *A&A* 325, 782
- Richards M. T. 1993, *ApJS*, 86, 255
- Rodonò M., Pagano I., Leto G. et al. 1999, *A&A* in press
- Schmitt J. H. M. M. 1994, *ApJS*, 90, 735
- Schmitt J. H. M. M., Favata F. 1999, *Nat* in press
- Schnopper H. W., Delvaille J. P., Epstein A. et al. 1976, *ApJ* 210, L75
- Singh K., Drake S., White N. 1995, *ApJ* 445, 840
- Stern R. A., Uchida Y., Tsuneta S., Nagase F. 1992, *ApJ* 400, 321
- Stern R. A., Lemen J. R., Schmitt J. H. M. M., Pye J. P. 1995, *ApJ* 444, L45
- Sylwester B., Sylwester J., Serio S. et al. 1993, *A&A* 267, 586
- Tsuboi Y., Koyama K., Murakami H. et al. 1998, *ApJ* 503, 894
- van den Oord G. H. J., Mewe R., Brinkman A. C. 1988, *A&A* 205, 181
- van den Oord G. H. J., Mewe R. 1989, *A&A* 213, 245
- Welsh B. Y., Vedder P. W., Vallergera J. V. 1990, *ApJ* 358, 473
- White N. E., Culhane J. L., Parmar A. N. 1986, *ApJ* 301, 262